Convection of heat and thermodynamic irreversibilities in two-phase, turbulent nanofluid flows in solar heaters by corrugated absorber plates

M. Akbarzadeh[a], S. Rashidi[a], N. Karimi[b], R. Ellahi[c,d,1]

[a] Department of Mechanical Engineering, Ferdowsi University of Mashhad, Mashhad 91775-1111, Iran

[b] School of Engineering, University of Glasgow, Glasgow G12 8QQ, UK

[c]Department of Mathematics & Statistics, FBAS, IIUI, Islamabad 4400, Pakistan

[d] Fulbright Fellow Department of Mechanical Engineering, UCR, CA 92521, USA

Abstract: The effects of simultaneous implementation of corrugated walls and nanoparticles upon the performance of solar heaters are investigated. Triangular and sinusoidal wall profiles along with varying concentration of nanoparticles are analyzed. The multi-phase mixture and the SST κ-ω models are used to simulate turbulent nanofluid flows inside the corrugated channels. The staggered computational grid is employed for storing the velocity and pressure terms at cell faces and cell center, respectively. The governing equations are first discretized by employing a second-order upwind differencing technique and are then solved by means of pressure-based finite volume approach. The convergence criterion is also presented for the validation of obtained results. The effects of wall profiles and nanoparticle concentration on the pertinent parameters including Nusselt number, pressure drop, performance evaluation criterion (PEC), and thermal and frictional irreversibilities are studied. This reveals that, in general, the triangular duct features superior heat transfer and inferior hydraulic characteristics in comparison with the

Corresponding author (R. Ellahi) e-mails: rellahi@alumni.ucr.edu, rahmatellahi@yahoo.com[1]

sinusoidal duct. It is demonstrated that as long as the base fluid (water) is used the highest value of PEC corresponds to the straight duct. Yet, by introducing nanofluids the PEC values of the corrugated ducts exceed those of the straight duct. The analysis further shows that on the basis of the performance evaluation criterion, the sinusoidal duct appears to be a better choice in comparison with the triangular duct. However, the situation is reversed when thermodynamic irreversibilities are considered. It is argued that vortex formation in the two investigated wavy walls and shear layer developed in the triangular case are the essential physical reasons for the observed thermal, hydraulic and entropic behaviors.

Keywords: Solar heater; Corrugated walls; Turbulent; Nanoparticles; Multi-phase mixture.

Nomenclature

a	Amplitude of wave (m)
$\vec{a}$	Nanoparticles acceleration (m s^{-2})
Be	Bejan number
C	Specific heat capacity (J kg^{-1} K^{-1})
d_f	Base liquid molecular size (nm)
d_p	Size of particles (nm)
D_ω^+	Positive segment of cross diffusion term
f_{drag}	Drag function
G_k	Creation of turbulent kinetic energy
G_ω	Creation of ω
h	Heat transfer factor (W m^{-2} K^{-1})
H	Channel height (m)

L_w	Wavelength of the wavy wall (m)
N_g	Non-dimensional positional volumetric entropy generation rate (Eq. 34 and 35)
Nu_{ave}	Average Nusselt number (Eq. 29)
p	Pressure (Pa)
Pr	Prandtl number
PEC	Performance evaluation criteria (Eq. 31)
q''	Heat flux (W m^{-2})
Re	Reynolds number (Eq. 28)
S_g'''	Entropy generation rate (W m^{-3} K^{-1})
T	Temperature (K)
u, v	Velocities in x and y axes (m s^{-1})
$\vec{V}_{dr,s}$	Drift velocity (m s^{-1})
x, y	Rectangular axes (m)

Greek symbols

α	Thermal diffusivity of liquid (m^2 s^{-1})
λ	Thermal conductivity (W m^{-1} K^{-1})
μ	Dynamic viscosity (kg $m^{-1}s^{-1}$)
$\mu_{t,m}$	Turbulent molecular viscosity
κ	Turbulent kinetic energy (m^2 s^{-2})
ω	Specific dissipation rate of turbulence kinetic energy (m^2 s^{-3})
ν	Kinematic viscosity (m^2 s^{-1})
ρ	Density of the fluid (kg m^{-3})

ΔP	Pressure drop (Pa)
ΔP^*	Dimensionless pressure drop (Eq. 30)
φ	Solid volume fraction
σ_k	Effective Prandtl number for turbulent kinetic
σ_ω	Effective Prandtl number for rate of dissipation

Subscripts/superscripts

f	Fluid
m	Mixture
in	Inlet
P	Particle
w	Wall
x	Local value

1. Introduction

Solar heaters are widely employed in low temperature applications wherein temperature gradients are relatively small and hence heat transfer potentials are limited. Example can be found in domestic sector for cloth laundering and bathing goals. Solar heaters devices are potentially inexpensive due to the simplicity of their configuration and ease of manufacturing. Further, they can utilize both direct and diffuse solar radiation to heat up a fluid flow. Nonetheless, the low heat transfer coefficient and the resultant requirement of high surface area remains as a major challenge for the design of solar heaters. As a result, currently there is a strong demand for the development of effective techniques to achieve ultra-performance in heat transfer rate of these devices. This problem has already attracted attention of the researchers from heat transfer and solar energy engineering communities. They have reported the

development of various passive techniques to improve the performance of different solar systems. Some of these passive techniques are addition of rough surfaces [1], inserting porous materials [2], mixing nanoparticles with the working fluid [3], adding swirl flow devices to enhance flow mixing [4] and implementing corrugated plates [5] for heat transfer improvement in solar systems. These have demonstrated varying levels of heat transfer enhancement with the expense of high pressure drop and sometimes higher levels of exergy destruction. As a result, the search for finding the optimal configurations and techniques of performance improvement remains ongoing.

It is now well demonstrated that nanofluids have substantial heat transfer capabilities due to their enhanced thermal conductivity in comparison with base fluids. This makes the use of nanofluids in thermal systems, including solar systems, most attractive. Mahian et al. [6] have reviewed the usages of nanofluids in solar systems. They introduced high production expenses, instability, augmentations of pressure drop and erosion as the critical challenges before the wide use of nanofluids in solar systems. Michael and Iniyan [7] evaluated the efficacy of CuO-water nanofluid in a solar water heater. They concluded that the thermal efficiency of the solar water heater enhanced by about 6.3% through using nanofluid with solid volume fraction of 0.05%. Kabeel et al. [8] studied experimentally the thermal performance of a solar water heater with Aluminum Oxide-water nanofluid. They observed that the outlet water temperature in the solar water heater enhanced by about 5.46% through using nanofluid with solid volume fraction of 2%. Chaw Sint et al. [9] evaluated theoretically the performance of a Copper Oxide/water nanofluid in a solar collector used for water heating. They reported that the influence of nanoparticle size on the efficiency of the system is marginal. Ebrahiminia-Bajestan et al. [10] performed both experimental and numerical works for nanofluid heat transfer characteristics for applications in solar heat exchangers. They concluded that the convective heat transfer

coefficient increases with an increase in the nanoparticle concentration and flow Reynolds number.

Some researchers have used other techniques to improve the thermal performance of solar heaters. Acir and Ata [11] improved the heat transfer in a new solar air heater by using circular type turbulators. They reported that the heat transfer and friction factor were improved by 416% and 511%, respectively in comparison with the conventional heater. Skullong et al. [12] used simultaneously corrugated groove and drilled-delta wing vortex generators inside a solar air heater. They concluded that simultaneous usage of the two techniques improved the thermal efficiency of the system between 37.7% and 46.3% larger than that obtained by the groove alone. Kumar et al. [13] investigated numerically the effects of roughened walls on the thermal performance of triangular duct solar air heater. They found that the heat transfer rate decreased through reducing the relative roughness, while it enhanced by increasing the relative roughness height on the internal surface of the duct. Sawhney et al. [14] used experimentally wavy delta winglets in a solar air heater. Their results indicated that heat transfer rate enhanced as the longitudinal pitch of the wavy delta winglets decreased. Bopche et al. [15] experimentally investigated the heat transfer and frictional specifications of a turbulator solar air heater duct with rough walls. They found that this duct improved the heat transfer and friction factor about 2.82 and 3.72 times, respectively comparing to the corresponding smooth duct.

A common feature of most of the cited literature is their sole focus on thermos-hydraulic aspects of the problem. However, the second law analysis is essential for each thermal system as the first law is only considered the conservation of energy and provides no data about destruction of the system exergy. Indeed, it has been shown that the second law analysis is a potent facility for the design, optimization and efficiency assessment of a wide range of thermal systems. Some researchers have conducted this analysis on different solar and thermal systems. Rashidi et al.

[16] carried out the second law study on a solar heat exchanger with a porous insert in laminar regime. They concluded that the entropy generation rate enhanced by reducing the Darcy numbers. Rashidi and Abolfazli Esfahani [17] conducted the second law analysis for a single slope solar still in laminar regime. These authors found that the still with larger aspect ratio has larger values of irreversibility. In their study, the aspect ratio was measured as the ratio of the still length and the still height. Bahaidarah and Sahin [18] investigated the second law characteristics of the fluid flow in a wavy duct. They showed that the height ratio of the duct has a great effect on the distribution of the irreversibility. Rashidi et al. [19] carried out an entropy generation study on the flow through a wavy duct. Their results indicated that the viscous entropy generation enhances by increasing the wave amplitude of the wavy wall. To get more understanding on the said topic, readers are referred to the studies [19-29].

The preceding review of literature discloses that some studies have already been conducted on the methods of heat transfer enhancement in solar heaters. To achieve further improvements in thermo-hydraulic and second law efficiencies of these devices, the current work combines two passive techniques of using nanofluid and wavy wall in solar heaters. To provide major novelty, the previous works in this area are advanced on two major fronts. First, in sharp contrast with the earlier investigations, a turbulent flow is considered in the current study. This allows for the inclusion of larger flow velocities and the heater configurations with sharp corners (triangular walls) in the analysis. It also offers a higher level of confidence about reproducibility of the results in the practical configurations. Second, a two-phase model of nanofluid is implemented in the numerical simulations, which provides a more realistic representation of the nanofluid as compared with the single phase models, frequently used in the earlier studies. A thermo-hydraulic analysis is conducted to assessment the influences of the combination of nanofluid and wavy walls on the heat transfer characteristics and pressure drop in the solar heaters. In addition,

an entropy generation analysis is put forward to assessment the second law efficiency of the investigated solar heaters.

2. Problem configuration and assumptions

A solar heater duct with the length of 20H and width of H as shown in Fig. 1 is considered. As discloses in this figure, a nanofluid flow with uniform and steady inlet velocity of U_{in} and inlet temperature of T_{in} enters the solar heater duct. Three duct geometries including triangular, sinusoidal, and straight configurations are simulated. The absorber plate of the heater is divided to three sections including the inlet and outlet parts with insulated surfaces and the mid-part, which is exposed to a constant heat flux representing the solar radiation. For the triangular and sinusoidal ducts, the mid-section of the absorber plate is wavy, while the whole absorber plate is smooth in the straight duct. The wavelength and the amplitude of the both wavy profiles are L_w=2H and a=0.2H, respectively. An insulated smooth surface is considered for the bottom walls of all three cases. Figure 2 shows the amplitude and wavelength of the corrugated profiles with close-up views of these cases.

The following assumptions are made throughout the current study.

- The nanofluid flow inside the duct is turbulent, incompressible, independent of time, and axisymmetric.
- The Reynolds number is varied in the range of $4000 \leq Re \leq 6000$.
- Cu-water nanofluid is considered as the working liquid. The multi-phase mixture model [30] is implemented to simulate the nanofluid flow. Table 1 shows the physical properties of the nanofluid [31].

3. Mathematical description

3.1. Governing equations

Considering the multi-phase mixture model [30], the governing equations of the nanofluid flow are:

- **Continuity equation:**

$$\nabla.\left(\rho_m \vec{V}_m\right) = 0 \tag{1}$$

- **Momentum equation:**

$$\nabla.\left(\rho_m \vec{V}_m \vec{V}_m\right) = -\nabla P_m + \nabla.\left[\mu_m \nabla \vec{V}_m - \sum_{s=1}^{n} \varphi_s \rho_s \bar{v}_s \bar{v}_s\right] + \nabla.\left(\sum_{s=1}^{n} \varphi_s \rho_s \vec{V}_{dr,s}\, \vec{V}_{dr,s}\right) \tag{2}$$

- **Energy equation:**

$$\nabla.\left[\sum_{s=1}^{n} \varphi_s \vec{V_s}(\rho_s H_s + P_m)\right] = \nabla.\left(\lambda_m \nabla T - C_p \rho_m \overline{vt}\right) \tag{3}$$

- **Volume fraction equation:**

$$\nabla.\left(\varphi_p \rho_p \vec{V}_m\right) = -\nabla.\left(\varphi_p \rho_p \vec{V}_{dr,p}\right) \tag{4}$$

The density, viscosity, and thermal conductivity of the mixture are defined by:

$$\rho_m = \sum_{s=1}^{n} \varphi_s \rho_s \tag{5}$$

$$\mu_m = \sum_{s=1}^{n} \varphi_s \mu_s \tag{6}$$

$$\lambda_m = \sum_{s=1}^{n} \varphi_s \lambda_s \tag{7}$$

The mass-average velocity $(\vec{V}_m)$ can be determined through the following expression:

$$\vec{V}_m = \sum_{s=1}^{n} \frac{\varphi_s \rho_s \vec{V}_s}{\rho_m} \tag{8}$$

The drift velocity $(\vec{V}_{dr,s})$ for the secondary phase s is calculated by,

$$\vec{V}_{dr,s} = \vec{V}_s - \vec{V}_m \tag{9}$$

The relative velocity, which is the velocity of the secondary phase (s) linked to the velocity of the primitive phase (f) is calculated by.

$$\vec{V}_{sf} = \vec{V}_s - \vec{V}_f \tag{10}$$

The drift velocity is a function of the relative velocity based on the following equation,

$$\vec{V}_{dr,s} = \vec{V}_{sf} - \sum_{s=1}^{n} \vec{V}_{fs} \frac{\varphi_s \rho_s}{\rho_m} \tag{11}$$

The equations below were suggested by Manninen et al. [32] and Schiller and Naumann [33] to define the relative velocity $(\vec{V}_{pf})$ and the drag function (f_{drag}):

$$\vec{V}_{pf} = \frac{\rho_p d_p^2}{18 \mu_f f_{drag}} \frac{\rho_p - \rho_m}{\rho_p} \vec{a} \tag{12}$$

$$f_{drag} = \begin{cases} 1 + 0.15 Re_p^{0.687} & Re_p \leq 1000 \\ 0.0183 Re_p & Re_p > 1000 \end{cases} \tag{13}$$

where $\vec{a}$ is the acceleration determined by

$$\vec{a} = -(\vec{V}_m . \nabla)\vec{V}_m \tag{14}$$

3.2. Turbulence modeling

In the present study, the Shear-Stress Transport (SST) $\kappa - \omega$ model of turbulence is used in conjunction with the multi-phase model of nanofluid. The transport equations for the turbulent kinetic energy (κ) and special loss rate of turbulence kinetic energy (ω) are given by [34, 35]:

$$\frac{\partial}{\partial x_i}\left(\rho_m \kappa V_{m,i}\right) = \frac{\partial}{\partial x_j}\left\{\left(\mu_m + \frac{\mu_{t,m}}{\sigma_k}\right)\frac{\partial \kappa}{\partial x_j}\right\} + G_k - \rho_m \kappa \omega \beta_1 \quad (15)$$

$$\frac{\partial}{\partial x_i}\left(\rho_m \omega V_{m,i}\right)$$

$$= \frac{\partial}{\partial x_j}\left\{\left(\mu_m + \frac{\mu_{t,m}}{\sigma_\omega}\right)\frac{\partial \omega}{\partial x_j}\right\} + G_\omega - \rho_m \omega^2 \beta_2 + 2(1 \quad (16)$$

$$- F_1)\rho_m \sigma_{\omega,2}\frac{1}{\omega}\frac{\partial \kappa}{\partial x_i}\frac{\partial \omega}{\partial x_i}$$

where G_k is the creation of turbulence kinetic energy as a result of the averaged velocity gradients, and G_ω is the production of ω. The turbulent viscosity $\left(\mu_{t,m}\right)$ is defined as:

$$\mu_{t,m} = \frac{\rho_m \kappa}{\omega}\frac{1}{max\left(\frac{1}{\alpha^*}, \frac{SF_2}{\alpha_1 \omega}\right)} \quad (17)$$

where F_1 and F_2 are the blending functions and S is the strain rate value. In equations (15) and (16), σ_k and σ_ω are the effective Prandtl numbers of the kinetic energy and special rate of loss respectively, which are defined as follows.

$$\sigma_\kappa = \frac{1}{\frac{F_1}{\sigma_{k,1}} + \frac{(1 - F_1)}{\sigma_{k,2}}}, \quad (18)$$

$$\sigma_\omega = \frac{1}{\frac{F_1}{\sigma_{\omega,1}} + \frac{(1 - F_1)}{\sigma_{\omega,2}}}. \quad (19)$$

The blending functions are calculated as,

$$F_1 = tanh(\phi_1^4), \quad (20)$$

$$F_1 = tanh(\phi_2^2), \quad (21)$$

where:

$$\phi_1 = min\left[max\left(\frac{\sqrt{\kappa}}{0.09\omega y}, \frac{500\mu}{\rho y^2 \omega}\right), \frac{4\rho\kappa}{\sigma_{\omega,2} D_\omega^+ y^2}\right], \quad (22)$$

$$D_{\omega}^{+} = max\left[2\rho\frac{1}{\sigma_{\omega,2}\omega}\frac{\partial\kappa}{\partial x_j}\frac{\partial\omega}{\partial x_j}10^{-20}\right], \tag{23}$$

$$\phi_2 = max\left[\left(\frac{2\sqrt{\kappa}}{0.09\omega y}\frac{500\mu}{\rho y^2\omega}\right)\right]. \tag{24}$$

where y is the near surface spacing and D_{ω}^{+} is the positive portion of the cross diffusion term. The constants of this model are $\sigma_{k,1} = 1.176$, $\sigma_{\omega,1} = 2$, $\beta_1 = 0.075$, $\beta_2 = 0.0828$, $\alpha_1 = 0.31$, $\sigma_{\kappa,2} = 1$ and $\sigma_{\omega,2} = 1.168$.

3.3. Boundary conditions

The boundary conditions of this problem are presented in this section.

- Inlet section of the heater (Uniform velocity and constant temperature):

$$u = U_{in},\ v = 0,\ T = T_{in}. \tag{25}$$

- Bottom and top walls of the heater (No-slip condition for the velocity field and fixed heat flux or adiabatic boundary condition for energy equation):

$$\begin{aligned} &u = 0,\ v = 0,\ \frac{\partial T}{\partial y} = q_w'' \quad \text{Wavy walls} \\ &u = 0,\ v = 0,\ \frac{\partial T}{\partial y} = 0 \quad \text{Smooth walls} \end{aligned} \tag{26}$$

- Outlet section of the heater (Neumann boundary conditions):

$$\frac{\partial u}{\partial x} = 0,\ \frac{\partial v}{\partial x} = 0,\ \frac{\partial T}{\partial x} = 0 \tag{27}$$

3.4. Parameter definition

The parameters employed in this study are presented in this section.

- Reynolds number:

$$\mathrm{Re} = \frac{\rho_f U_{in} H}{\mu_f} \tag{28}$$

- Mean Nusselt number:

$$Nu_{ave} = \frac{q'' H}{\left(\overline{T}_w - T_{in}\right)\lambda_f} \tag{29}$$

where $\overline{T}_w$ shows the average temperature of the absorber plate.

- Pressure loss in the dimensionless form is given by

$$\Delta P^* = \frac{\Delta P}{\rho U_{in}^2} \tag{30}$$

where ΔP is the pressure loss.

- Performance evaluation criteria:

Webb and Kim [36] discussed the performance evaluation criteria (PEC) for the single-phase heat exchanging systems with different objective function and constraints and defined it for 12 different cases. They derived the following equation

$$\frac{hA/h_s A_s}{(P/P_s)^{1/3}(A/A_s)^{2/3}} = \frac{j/j_s}{(f/f_s)^{1/3}}, \tag{31}$$

where h is heat transfer coefficient, A is heat transfer surface area, P is pumping power, j is heat transfer factor ($St.Pr^{\frac{2}{3}}$), and f represents fanning friction factor. One of the variables on the left side of the equation is set as the objective function, and the remaining two are set as the operating constraints, with the value 1.0 [36]. On the basis of Ref. [36], in the current study, the following equation is used to determine the thermal hydraulic performance of different channels with varying nanoparticle volume fractions [37]:

$$PEC = \frac{Nu_{wavy\ heater} \Big/ Nu_{straight\ heater,base\ fluid}}{\left(\Delta P_{wavy\ heater} \Big/ \Delta P_{straight\ heater,base\ fluid}\right)^{1/3}} \tag{32}$$

- Local volumetric viscous entropy generation rate [37]:

$$S'''_{g,fr} = \frac{\mu}{T}\left\{2\left[\left(\frac{\partial u}{\partial x}\right)^2 + \left(\frac{\partial v}{\partial y}\right)^2\right] + \left[\left(\frac{\partial u}{\partial y}\right) + \left(\frac{\partial v}{\partial x}\right)\right]^2\right\} \quad (33)$$

- Local volumetric thermal entropy generation rate [37]:

$$S'''_{g,\,th} = \frac{\lambda}{T^2}\left[\left(\frac{\partial T}{\partial x}\right)^2 + \left(\frac{\partial T}{\partial y}\right)^2\right] \quad (34)$$

- Non-dimensional volumetric viscous entropy generation rate:

$$N^*_{fr} = \frac{S'''_{g,\,viscous} H^2}{\lambda} \quad (35)$$

- Non-dimensional volumetric thermal entropy generation rate:

$$N^*_{th} = \frac{S'''_{g,\,thermal} H^2}{\lambda} \quad (36)$$

- Non-dimensional entropy generation rate per unit depth:

$$N = \frac{1}{A}\left[\int_A (N^*) dA\right] \quad (37)$$

where A is the surface of the heater.

3.5. Numerical procedure

All equations are solved by employing a pressure-based finite volume approach. The staggered computational grid is employed for storing the velocity and pressure terms at cell faces and cell center, respectively. In addition, the SIMPLE algorithm [38] provides the coupling between the velocity and pressure terms. All equations are discretized by employing a second-order upwind differencing technique. Eventually, the convergence criteria for all equations are passed for sum of the residuals lower than 10^{-6}.

3.6. Grid independency test and validations

Figure 3 discloses a sample grid distribution inside the heater for all three cases. A square grid with high density near top absorber and bottom walls of the heater, where temperature and velocity gradients are intense was generated. A grid independency study was arranged to achieve the reliable results that are independent of the grid size. Accordingly, figure 4 shows the effect of mesh size on the mean Nusselt number and pressure drop for the sinusoidal duct with $\varphi = 0.04$. The differences in the mean Nusselt number and pressure drop between grid numbers of 60×2000 and 80×2400 are 0.95% and 0.93%, respectively. Thus, the grid number of 60×2000 was used for production of the rest of the results in the present study.

To examine the precision of the numerical procedure, the current numerical findings were compared with the experimental and theoretical findings of previous researches. Figure 5 shows the comparison between the present numerical results and those from the theoretical study of Dittus and Boelter [39] for turbulent flow in a straight pipe. This figure shows that there is an excellent matching between the two sets of results. In addition, Table 2 presents a comparison between the current numerical findings and the experimental data of Ahmed et al. [40] for nanofluid flow at $\varphi = 0.01$ in a corrugated duct. This comparison indicates that there is fine matching between the experimental and numerical results with an average percentage difference of less than 13%, which has been commonly reported in the literature [41].

4. Results and discussion

The results of numerical simulations are presented and discussed in this section. The effects of different wavy profiles, Reynolds numbers and nanoparticle concentrations on different characteristics of the system including heat transfer, pressure drop, PEC, and thermal and frictional irreversibilities are investigated.

4.1. Hydrodynamics and First law of thermodynamics analyses

Figures 6 and 7 disclose the average velocity vectors and streamlines for triangular, sinusoidal, and straight ducts. The velocity vectors are plotted at different sections. As shown in Fig. 6, a reverse flow occurs in the cavities near surface of the wavy duct. However, as expected, no reverse flow develops within the straight duct. The flow reversal has an ability to generate secondary recirculation flows. These recirculation flows are clearly visible around the crest area of each wave of the triangular and sinusoidal ducts. It should be noted that the flow disturbances are noticeably stronger at recirculation regions. As will be demonstrated later, these disturbances contribute with the heat transfer enhancement and also viscous irreversibilities.

Figure 8 shows the variations of mean Nusselt number with nanoparticle concentrations for different duct profiles at Re=5000. In general, the wavy ducts have the higher values of Nusselt number in comparison with the straight duct. As shown in Fig. 7, some large scale vortices are formed inside the cavities near the surfaces of wavy ducts. These vortices enhance the mixing of nanofluid and hence improve the heat transfer rate inside the duct. Figure 8 indicates that among the investigated configurations, the triangular duct provides a marginally higher Nusselt number in comparison with the sinusoidal one. Sharp corners of the triangular disturb the flow strongly through generation of a shear layer, which leads to significant mixing and heat transfer improvement. In addition, the Nusselt number enhances by using the nanofluid and increasing the nanoparticles‘ concentration. This may be explained by noting that the thermal conductivity of the mixture increase through substantiating nanoparticles concentration.

Figure 9 discloses the changes of dimensionless pressure drop with increasing the nanoparticles concentration for different ducts at Re=5000. It is clear from this figure that the wavy ducts feature stronger pressure drop penalty in comparison with a straight duct. Inverse flows generated by the wavy walls enhance the pressure drop through dissipating the kinetic energy of the flow in vortical structures. As shown in Fig. 6, there is a regular flow pattern without inverse

flows in the straight duct, which results in lower pressure drop penalty in this configuration. As already discussed, between the wavy ducts, the triangular duct has the highest pressure drop penalty. The pressure drop increases by switching to nanofluid and substantiates by augmenting the concentration of nanoparticles. This behaviour is more noticeable in wavy ducts in comparison with the straight duct. Generally, a nanofluid with large concentration of nanoparticles has a higher viscosity in comparison with the base fluid and this increases the friction forces and magnifies the pressure drop in the duct. Figure 9 shows that the non-dimensional pressure drop increases by about 61% by increasing the nanoparticle concentration in the range of 0 to 0.04 for the case of triangular duct. This value is about 56% and 24% for the sinusoidal and straight ducts, respectively.

4.2. Second law of thermodynamics analysis

Figure 10 shows the variations of non-dimensional thermal entropy generation with nanoparticle concentrations for different ducts at Re=5000. The thermal entropy generation decreases by using the wavy wall in comparison with the straight duct. As discussed earlier, the heat transfer rate increases by implementing the wavy ducts and hence, the temperature discrepancy between the duct wall and the bulk flow decreases. This is due to the fact that the walls of the system are exposed to a constant heat flux. A lower temperature difference leads to a reduction in the thermal irreversibility within the heat transferring flow. Figure 10 shows that the triangular duct has a lower thermal irreversibility in comparison with the sinusoidal duct. This is because of the higher values of heat transfer rates in the triangular duct. The thermal irreversibility decreases by about 31% by using a wavy duct with triangular absorber wall in comparison with the straight wall at φ=0.01. Finally, it is observed that the thermal irreversibility decreases by using the nanofluid and increasing the nanoparticle concentration. Improvements in heat transfer caused by

using the nanofluid, particularly that with high concentration of nanoparticles, are responsible in this decrease in the irreversibility of the system. The thermal irreversibility decreases by about 79% through using the nanofluid with φ=0.04 for straight duct. These reductions are about 108% and 104% for triangular and sinusoidal ducts, respectively.

Figure 11 depicts the variations of non-dimensional frictional entropy generation with nanoparticle concentrations for different ducts. It is clear from this figure that the frictional entropy generation increases by using the wavy wall in comparison with the straight duct. As discussed earlier, wavy wall generate flow disturbances. Further, implementation of wavy wall leads to the formation of throat zones in the duct, which impose higher resistance against the flow and cause larger frictional irreversibility. In between triangular and sinusoidal walls, the triangular duct features a larger frictional irreversibility, which is due to the effects of the sharp corners of the triangular duct on the flow field. Figure 11 shows that at φ=0.01 the frictional irreversibility increases by about 34% through using a triangular absorber wall in comparison with that of the straight wall. Finally, it is observed that the use of nanofluid and increasing the nanoparticles' concentration result in magnification of the frictional irreversibility. This can be explained by noting that the viscosity of nanofluid increases by increasing the nanoparticles' concentration, and therefore intensifies the flow friction. In the case of straight duct, the frictional irreversibility increases by about 24% by increasing the concentration of nanoparticles from φ=0.0 to φ=0.04. This increment is about 33% for both triangular and sinusoidal ducts, reflecting the pronounced influences of wavy walls on the flow friction.

Figure 12 shows the non-dimensional thermal entropy generation contours for triangular, sinusoidal, and straight ducts for φ=0 and 0.04 at Re=5000. As shown in this figure, thermal irreversibility reaches its maximum value near the top absorber plate for all cases as this wall is exposed to the heat flux. Expectedly, however, the thermal irreversibility is almost zero around

the adiabatic bottom wall. For triangular and sinusoidal ducts, there is a region in each diverging section of the wavy wall with a small value of thermal irreversibility. As shown in Fig. 7, a recirculation region forms in the diverging sections of the wavy wall. This prevents contact between the fluid and the hot surface and hence decreases the temperature gradient in the nanofluid. As a result, the thermal irreversibility drops significantly in this region. Finally, the thermal irreversibility decreases with increasing the nanoparticle concentration. This is arising from the increases in the thermal conductivity of the nanofluid, which tends to relax the temperature gradients and reduce the thermal irreversibility.

Figure 13 discloses the non-dimensional frictional entropy generation contours for triangular, sinusoidal, and straight ducts for the same conditions as Fig. 12. It can be seen in this figure that the numerical value of local frictional irreversibility grows noticeably near the top and bottom walls, which is due to the existence of intense flow velocity gradients in these areas. For triangular and sinusoidal ducts, the frictional entropy generation is larger around the throat regions of the wavy wall. As already discussed, these regions generate strong resistance against the flow and cause a larger frictional irreversibility. It is further clear that with increasing the nanoparticles' concentration the frictional irreversibility influences a larger volume of the nanofluid. In Fig. 13, it can be seen that for $\varphi = 0$, although the maximum values of frictional entropy generation occur in the concave parts of the channel, in the convex parts of both wavy profiles there are regions without any frictional entropy generation. For $\varphi = 0.04$, the maximum values of frictional entropy generation are almost the same as $\varphi = 0$ both in terms of quantity and location. The most visible difference is that for $\varphi = 0.04$ there are frictional entropy generations in concave areas, which cause higher total frictional irreversibility. It is observed that in Fig. 13 that the location and maximum value of entropy generation has remained almost unchanged with the increase in the concentration of nanoparticles. This could be explained by

first noting that, in the investigated configuration, frictional entropy is predominately generated within the shear layer formed at the back of the trough points of the wavy walls, which is fixed for a given wall geometry. Second, increasing the nanoparticle concentration boosts the viscosity. Although this is expected to enhance the frictional irreversibility, it also increases the resistance of the nanofluid to form vortices in the shear layer. The two counter effects seem to mostly neutralize each other and thus the maximum value of entropy generation remains constant. Nevertheless, the more viscous nanofluid produces a larger area with finite shear stress enlarging the spatial extent of the frictional entropy generation and resulting in the larger overall frictional irreversibility.

Figure 14 shows the Bejan number contours at $\varphi=0.04$ for triangular, sinusoidal, and straight ducts at Re=5000. Bejan number is presented as the ratio of the thermal entropy to total one including thermal and viscous entropies. As shown in this figure, for all ducts the thermal irreversibility is dominant around the top absorber wall as a result of the high temperature gradients at that part of the system. The thickening layer of high Bejan number approximately represents the thermal boundary layer. This grows along the duct length and becomes thicker and occupies most of the channel at around the exit point. The intense temperature gradient inside this layer substantiates the thermal irreversibility and hence magnifies the Bejan number. The frictional irreversibility, however, is only dominated at the entrance of the channel due to the existence of large velocity gradients in the developing flow area.

4.3 First and second laws design considerations

The analyses presented in sections 4.1 and 4.2 were concerned with the physical processes that dominate the rate of heat transfer, pressure loss and entropy generation in different duct configurations. It was shown that, in general, the use of wavy walls improves the rate of heat transfer, while it also intensifies the pressure drop and entropy generation. These pieces of

information, although physically insightful, can be difficult to use for design purposes. To resolve this issue, a set of parametric studies is conducted in this section. The aim is to compare the two investigated wavy ducts from thermohydraulic and second law viewpoints and to make design recommendations.

Figure 15 shows variations of the Performance Evaluation Criterion (PEC), as defined by Eq. (31), with increases in the nanoparticles concentration for different ducts at Re=5000. It should be recalled that to make an accurate conclusion about the overall performance of each thermal system, it is necessary to assessment the heat transfer and pressure drop in a system, simultaneously. A performance evaluation criterion (PEC) provides this opportunity for the designer to select the best case on the basis of the specific problem in hand. As shown in Fig.15, PEC enhances by increasing the nanoparticle concentration for all ducts. Therefore, it can be understood that for all designs, utilization of nanofluid features much more desirable effects on the heat transfer enhancement than the adverse effects on the pressure drop. For example, the PEC values enhance by about 61%, 71%, and 72% by increasing the nanoparticle concentration in the range of 0 to 0.04 for the straight, triangular, and sinusoidal ducts, respectively. Ahmed et al [42,43] showed that the PEC for wavy channels increases with an increase in the nanoparticle volume fraction for the laminar regime. As shown in Fig.15, the wavy ducts have higher values of PEC in comparison with the straight one for the cases in which nanofluid has been used. However, the straight duct has a higher PEC in comparison with the wavy ducts for the case of pure water ($\varphi=0$). Further, between the two investigated wavy ducts, the sinusoidal duct has a marginally higher PEC in comparison with the triangular one. As shown in Fig. 9, the pressure drop of the triangular duct is higher than the sinusoidal one because of the sharp corners in the triangular profile. This is the main reason of lower PEC for triangular duct in comparison with

the sinusoidal duct. Ahmed et al [42] also showed that for laminar regime the values of PEC for triangular profile are lower than the sinusoidal duct.

These are important findings from the design point of view. It is intuitively predictable that the wavy walls magnify the pressure drop and enhance the rate of heat transfer. It is also physically expected that adding nanoparticles increases the heat transfer rate and pressure drop. The results presented in this section quantified these trends. However, these pieces of information are insufficient and even confusing for the design of solar systems, which take advantage of both nanofluid and wavy walls. The PEC values, given by Fig. 15, provide the missing bit of information. Calculation of PEC is only possible through the current detailed analyses of the flow and clearly the accurate modelling of nanofluid and flow conducted in Section 3.

Table 3 presents the influences of Reynolds number on heat transfer, pressure drop, PEC, and thermal and frictional irreversibilities for triangular and sinusoidal channels. Three different values of Reynolds number, Re=4000, 5000, 6000, and two different values of nanoparticles' concentration, φ=0.01 and φ=0.04, have been used in this table. It is evident that for both wavy ducts, by increasing the value of Reynolds number the numerical values of Nusselt number and pressure drop grow. The same trend is observed when the concentration of nanoparticles increases. Further, a comparison between the values of Nusselt number associated with the triangular duct and the corresponding values for sinusoidal duct shows that for all cases triangular duct features a slightly higher value of Nusselt number. However, the difference between the numerical values of the pressure drop calculated for triangular and sinusoidal ducts is more noticeable. Hence, the PEC values for sinusoidal duct are generally higher than those of triangular duct. This difference is almost negligible for φ=0.01 but it becomes more considerable at φ=0.04. This result along with those presented by Fig. 15 indicate that as far as thermohydraulics are concerned, a sinusoidal wall profile is superior to a triangular one. This is

particularly the case when high concentrations of nanoparticles are used in the system. However, the situation is quite different when the second law considerations are taken into account. First, Table 3 (and also section 4.2) indicates that the total entropy generation is globally dominated by the thermal entropy and the viscous irreversibility is always smaller than the thermal irreversibilities by orders of magnitude. Second, the thermal irreversibility of the system with sinusoidal walls is constantly larger than that of triangular walls. This means that from the view point of entropy generation minimization, the triangular walls are preferred to the sinusoidal profiles.

Contradicting rankings generated by first and second law analyses are rather common and have been reported frequently in the literature. It follows that the final design decision is somehow subjective and depends upon the specific weighting that the designer gives to first and second law aspects of the problem.

5. Conclusions

In this paper, the first and second laws of thermodynamics analyses were performed on nanofluid turbulent flows in a solar heater with the wavy absorber plate. The effects of wavy profiles and nanoparticle concentration on different parameters including heat transfer, pressure drop, PEC, and thermal and frictional irreversibilities were investigated. The main results of this work are summarized as follows.

- The reverse flow with secondary recirculation region is formed in cavities near the surface of wavy duct, while there is a regular flow for the straight duct. This reversal flow has an ability to mix the fluid and improve the heat transfer rate.
- Among the wavy ducts, the triangular duct provides a marginal higher Nusselt number as compared with the sinusoidal one.

- Among the wavy ducts, the triangular duct has a higher pressure drop penalty as compared with the sinusoidal one.
- The wavy ducts have higher PEC as compared with the straight duct for the case of nanofluid. However, the straight duct has a higher PEC in comparison with the wavy ducts for the case of pure water ($\varphi=0$).
- PEC enhances by increasing the nanoparticle concentration for all ducts. For example, PEC values enhance by about 61%, 71%, and 72% by increasing the nanoparticle concentration in the range of 0 to 0.04 for the straight, triangular, and sinusoidal ducts.
- PEC decreases by increasing the Reynolds number.
- The thermal entropy generation reduces by using the wavy wall as compared with the straight duct.
- The thermal irreversibility decreases about 79% by using the nanofluid with $\varphi=0.04$ for straight duct. These reductions are about 108% and 104% for triangular and sinusoidal ducts, respectively. Among the wavy ducts, the triangular duct has a larger frictional irreversibility in comparison with the sinusoidal one.
- The frictional irreversibility increases by about 34% by using a wavy duct with triangular absorber wall in comparison with the straight wall at $\varphi=0.01$.
- The maximum thermal irreversibility occurs around top absorber plate for all cases as this wall is exposed to the external heat flux.
- The maximum frictional irreversibility occurs near the top and bottom walls due to the large values of velocity gradients at these regions.
- The thermal entropy generation reduces by increasing the Reynolds number, while the frictional entropy generation increases as the Reynolds number increases.

- The thermal irreversibility is dominant around top absorber wall for all ducts due to the high temperature gradients at the top wall.
- The frictional irreversibility is dominated at the entrance of the channel due to the high velocity gradients.

References

[1] V. S. Bisht, A. K. Patil, A. Gupta, "Review and performance evaluation of roughened solar air heaters.'' Renewable and Sustainable Energy Reviews 81 (2018) 954–977.

[2] S. Rashidi, J.A. Esfahani, A. Rashidi, "A review on the applications of porous materials in solar energy systems." Renewable and Sustainable Energy Reviews, 73 (2017) 1198-1210.

[3] A. Kasaeian, A. Toghi Eshghi, M. Sameti, "A review on the applications of nanofluids in solar energy systems." Renewable and Sustainable Energy Reviews, 43 (2015) 584–598.

[4] A. Saravanan, J.S. Senthilkumaar, S. Jaisankar, ''Performance assessment in V-trough solar water heater fitted with square and V-cut twisted tape inserts.'' Applied Thermal Engineering 102 (2016) 476-486

[5] A. Priyam, P. Chand, "Thermal and thermohydraulic performance of wavy finned absorber solar air heater." Solar Energy, 130 (2016) 250–259.

[6] O. Mahian, A. Kianifar, S.A. Kalogirou, I. Pop, S. Wongwises, "A review of the applications of nanofluids in solar energy." International Journal of Heat and Mass Transfer, 57 (2013) 582–594.

[7] J.J. Michael, S. Iniyan, "Performance of copper oxide/water nanofluid in a flat plate solar water heater under natural and forced circulations." Energy Conversion and Management, 95 (2015) 160–169.

[8] A. E. Kabeel, E.M.S. El-Said, M. Abdulaziz, “Thermal solar water heater with H_2O-Al_2O_3 nanofluid in forced convection: Experimental investigation.” International Journal of Ambient Energy, 38 (2017) 85-93.

[9] N.K. Chaw Sint, I.A. Choudhury, H.H. Masjuki, H. Aoyama, “Theoretical analysis to determine the efficiency of a CuO-water nanofluid based-flat plate solar collector for domestic solar water heating system in Myanmar.” Solar Energy, 155 (2017) 608-619.

[10] E. Ebrahimnia-Bajestan, M. CharjoueiMoghadam, H. Niazmand, W. Daungthongsuk, S. Wongwises, “Experimental and numerical investigation of nanofluids heat transfer characteristics for application in solar heat exchangers.” International Journal of Heat and Mass Transfer, 92 (2016) 1041-1052.

[11] A. Acır, İ. Ata, “A study of heat transfer enhancement in a new solar air heater having circular type turbulators.” Journal of the Energy Institute, 89 (2016) 606-616.

[12] S. Skullong, P. Promvonge, C. Thianpong, M. Pimsarn, “Thermal performance in solar air heater channel with combined wavy-groove and perforated-delta wing vortex generators.” Applied Thermal Engineering, 100 (2016) 611-620.

[13] R. Kumar, A. Kumar, V. Goel, “A parametric analysis of rectangular rib roughened triangular duct solar air heater using computational fluid dynamics.” Solar Energy 157 (2017) 1095–1107.

[14] J.S. Sawhney, R. Maithani, S. Chamoli, “Experimental investigation of heat transfer and friction factor characteristics of solar air heater using wavy delta winglets.” Applied Thermal Engineering, 117 (2017) 740-751.

[15] S. B. Bopche, M.S.Tandale, “Experimental investigations on heat transfer and frictional characteristics of a turbulator roughened solar air heater duct.” International Journal of Heat and Mass Transfer, 52 (2009) 2834-2848.

[16] S. Rashidi, M. Bovand, J.A. Esfahani, “Sensitivity analysis for entropy generation in porous solar heat exchangers by RSM.’’ Journal of Thermophysics and Heat Transfer, 31 (2017) 390-402.

[17] S. Rashidi, J.A. Esfahani, “Spatial entropy generation analysis for the design improvement of a single slope solar still.” Environmental Progress & Sustainable Energy, Accepted (2017), DOI: 10.1002/ep.12719.

[18] H.M.S. Bahaidarah, A.Z. Sahin, “Thermodynamic analysis of fluid flow in channels with wavy sinusoidal walls.” Thermal Science, 17 (2013) 813-822.

[19] S. Rashidi, M. Akbarzadeh, R. Masoodi, E.M. Languri, “Thermal-hydraulic and entropy generation analysis for turbulent flow inside a corrugated channel.’’ International Journal of Heat and Mass Transfer, 109 (2017) 812-823.

[20] M.A. Sheremet, I. Pop, O. Mahian, Natural convection in an inclined cavity with time-periodic temperature boundary conditions using nanofluids: Application in solar collectors, International Journal of Heat and Mass Transfer, 116 (2018), 751-761

[21] M. Mamourian, K. Milani Shirvan, R. Ellahi, A.B. Rahimi, Optimization of mixed convection heat transfer with entropy generation in a wavy surface square lid-driven cavity by means of Taguchi approach, International Journal of Heat and Mass Transfer, 102 (2016) 544-554.

[22] H. Khosravi Bizhaem, A. Abbassi, Numerical study on heat transfer and entropy generation of developing laminar nanofluid flow in helical tube using two-phase mixture model, Advanced Powder Technology, 28 (9) (2017), 2110-2125.

[23] K. Milani Shirvan, R. Ellahi, M. Mamourian and M. Moghiman, Effect of wavy surface characteristics on heat transfer in a wavy square cavity filled with nanofluid, International Journal of Heat and Mass Transfer, 107 (2017) 1110–1118.

[24] M. Siavashi, R. Yousofvand, S. Rezanejad, Nanofluid and porous fins effect on natural convection and entropy generation of flow inside a cavity, Advanced Powder Technology, 29 (1) (2018), 142-156.

[25] H. Safikhani, F. Abbasi, Numerical study of nanofluid flow in flat tubes fitted with multiple twisted tapes, Advanced Powder Technology, 26 (6) (2015), 1609-1617.

[26] M. I. A. Othman, M. Marin, Effect of thermal loading due to laser pulse on thermoelastic porous medium under G-N theory, Results in Physics, 7 (2017), 3863-3872.

[27] Dharmendra Tripathi, Ashish Sharma, O. Anwar Bég, Electrothermal transport of nanofluids via peristaltic pumping in a finite micro-channel: Effects of Joule heating and Helmholtz-Smoluchowski velocity, International Journal of Heat and Mass Transfer, 111(2017), 138-149.

[28] M. Bahiraei, M. Jamshidmofid, S. Heshmatian, Entropy generation in a heat exchanger working with a biological nanofluid considering heterogeneous particle distribution, Advances Powder Technology, 28 (9) (2017), 2380-2392.

[29] M. Torabi, G.P. Peterson, Effects of velocity slip and temperature jump on the heat transfer and entropy generation in micro porous channels under magnetic field, International Journal of Heat and Mass Transfer, 102 (2016), 585-595.

[30] G. Saha, M. C. Paul, "Heat transfer and entropy generation of turbulent forced convection flow of nanofluids in a heated pipe." International Communications in Heat and Mass Transfer, 61 (2015) 26–36.

[31] M. Akbarzadeh, S. Rashidi, M. Bovand, R. Ellahi, "A sensitivity analysis on thermal and pumping power for the flow of nanofluid inside a wavy channel." Journal of Molecular Liquids, 220 (2016) 1-13.

[32] M. Manninen, V. Taivassalo, S. Kallio, “On the mixture model for multiphase flow.” Tech. Res. Cent. Finl. 288 (1996) 9–18.

[33] L. Schiller, A. Naumann, “A drag coefficient correlation.” Z. Ver. Deutsch. Ing. 77 (1935) 318–320.

[34] G. Saha, M. C. Paul, “Analysis of Heat Transfer and Entropy Generation of TiO2-Water Nanofluid Flow in a Pipe under Transition.” Procedia Engineering 105 (2015) 381 – 387.

[35] F.R. Menter, “Two-equation eddy-viscosity turbulence models for engineering applications.” J. AIAA 32 (1994) 1598-1605.

[36] R.L. Webb, N.H. Kim, Principles of heat transfer enhancement, second ed., Taylor and Francis Group, New York, 2005.

[37] M. Akbarzadeh, S. Rashidi, J.A. Esfahani, “Influences of corrugation profiles on entropy generation, heat transfer, pressure drop, and performance in a wavy channel.” Applied Thermal Engineering, 116 (2017) 278–291.

[38] S. V. Patankar, Numerical Heat Transfer and Fluid Flow, Hemisphere, New York,1980.

[39] A. Bejan, Convection Heat Transfer, fourth ed., John Wiley and Sons, Inc., Hoboken, New Jersey, 2013.

[40] M.A. Ahmed, M.Z. Yusoff, K.C. Ng, N.H. Shuaib, Numerical and experimental investigations on the heat transfer enhancement in corrugated channels using SiO_2-water nanofluid.’’ Case Studies in Thermal Engineering, 6 (2015) 77–99.

[41] N. Rahbar, J. A. Esfahani, E. Fotouhi-Bafghi, “Estimation of convective heat transfer coefficient and water-productivity in a tubular solar still – CFD simulation and theoretical analysis.” Solar Energy 113 (2015) 313-323.

[42] M.A. Ahmed, M.Z. Yusoff, K.C. Ng, N.H. Shuaib, "Effect of corrugation profile on the thermal-hydraulic performance of corrugated channels using CuO-water nanofluid." Case Studies in Thermal Engineering, 4 (2014) 65-75.

[43] M.A. Ahmed, M.Z. Yusoff, K.C. Ng, N.H. Shuaib, "The effects of wavy-wall phase shift on thermal-hydraulic performance of Al_2O_3–water nanofluid flow in sinusoidal-wavy channel." Case Studies in Thermal Engineering, 4 (2014) 153–165.

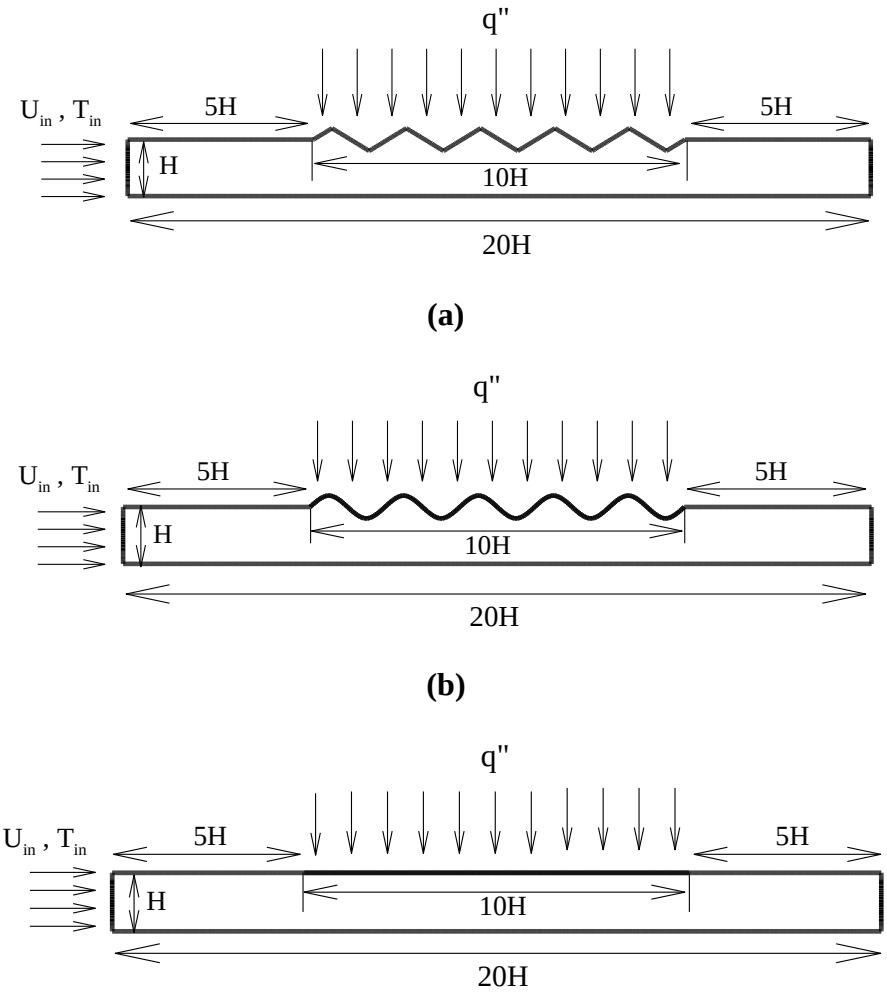

Fig. 1. Geometry definition for (a) triangular duct; (b) sinusoidal duct; (c) straight duct

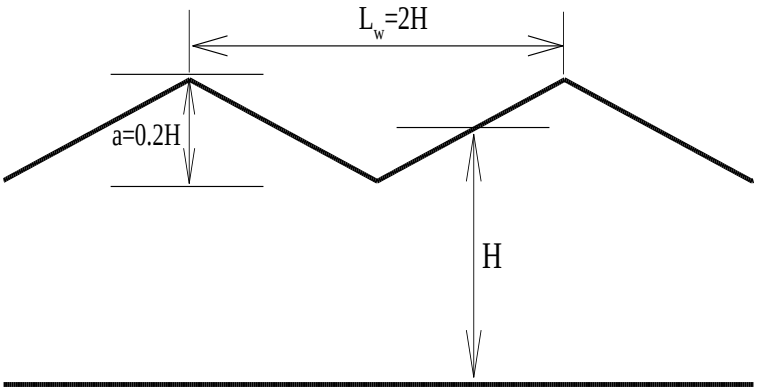

(a)

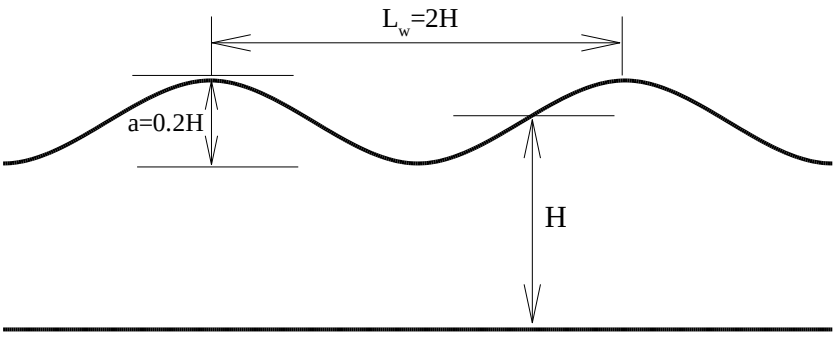

(b)

Fig. 2. Amplitude and wavelength of corrugated profiles with a close-up view for (a) triangular channel; (b) sinusoidal channel

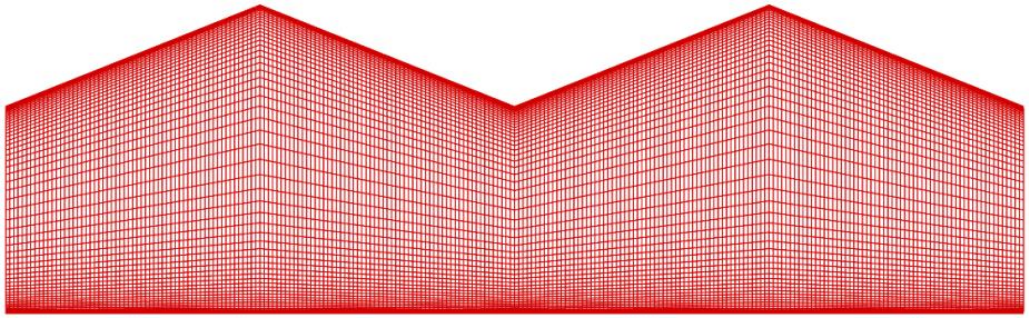

(a)

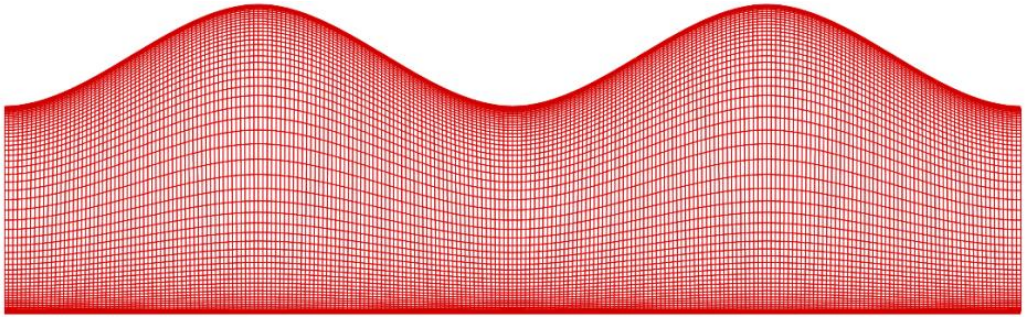

(b)

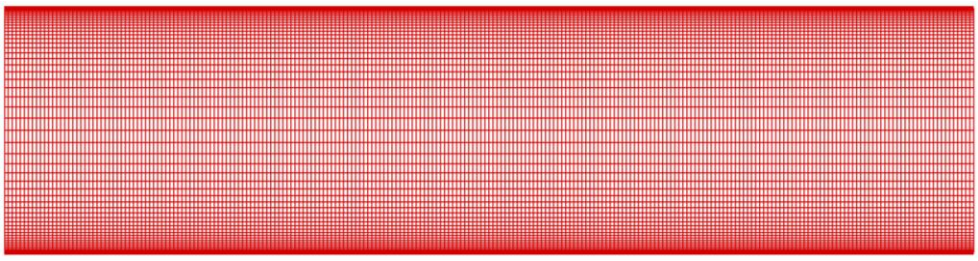

(c)

Fig. 3. Sample grid distribution inside the heater for (a) triangular duct; (b) sinusoidal duct; (c) straight duct

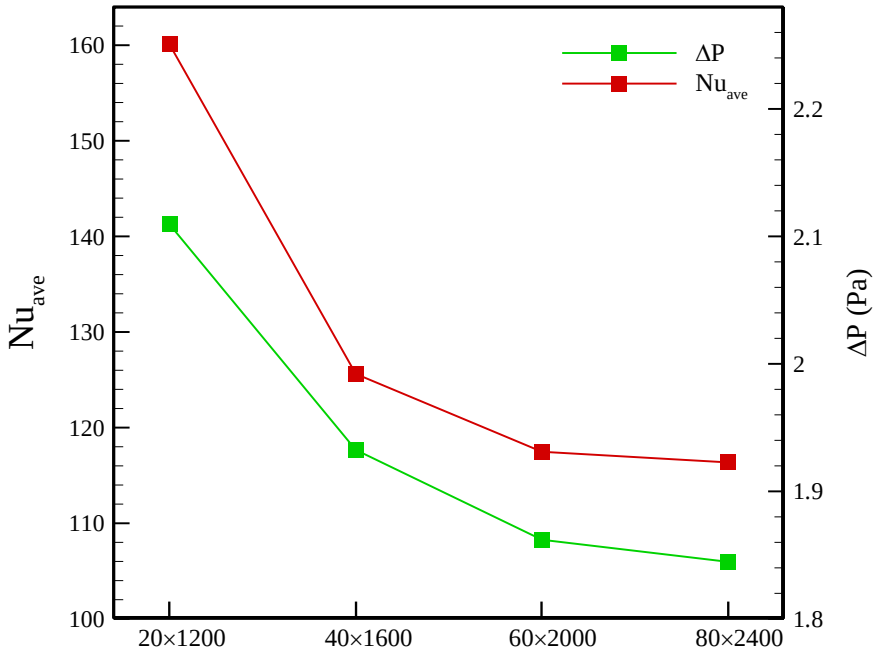

Fig. 4. Effect of mesh size on the average Nusselt number and pressure drop for sinusoidal duct at $\varphi = 0.04$ and Re=5000.

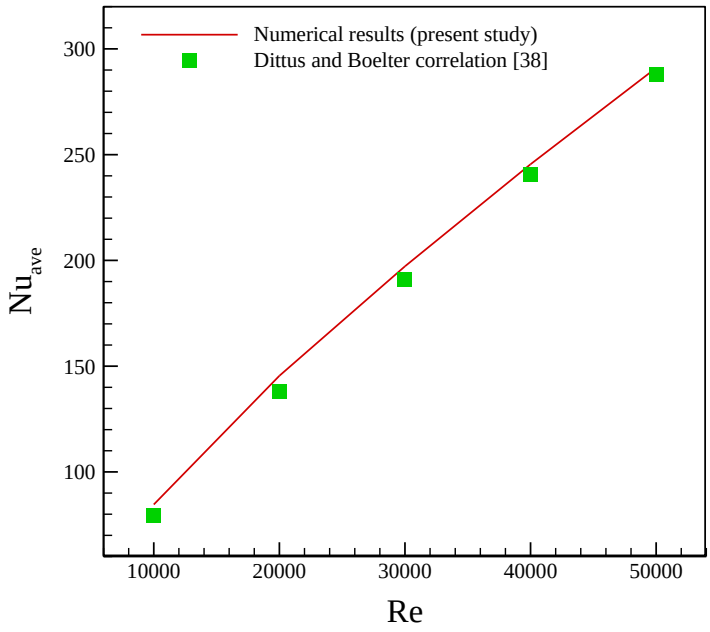

Fig. 5. Comparison between the present numerical results and theoretical results of Dittus and Boelter [38] for turbulent flow in a straight pipe

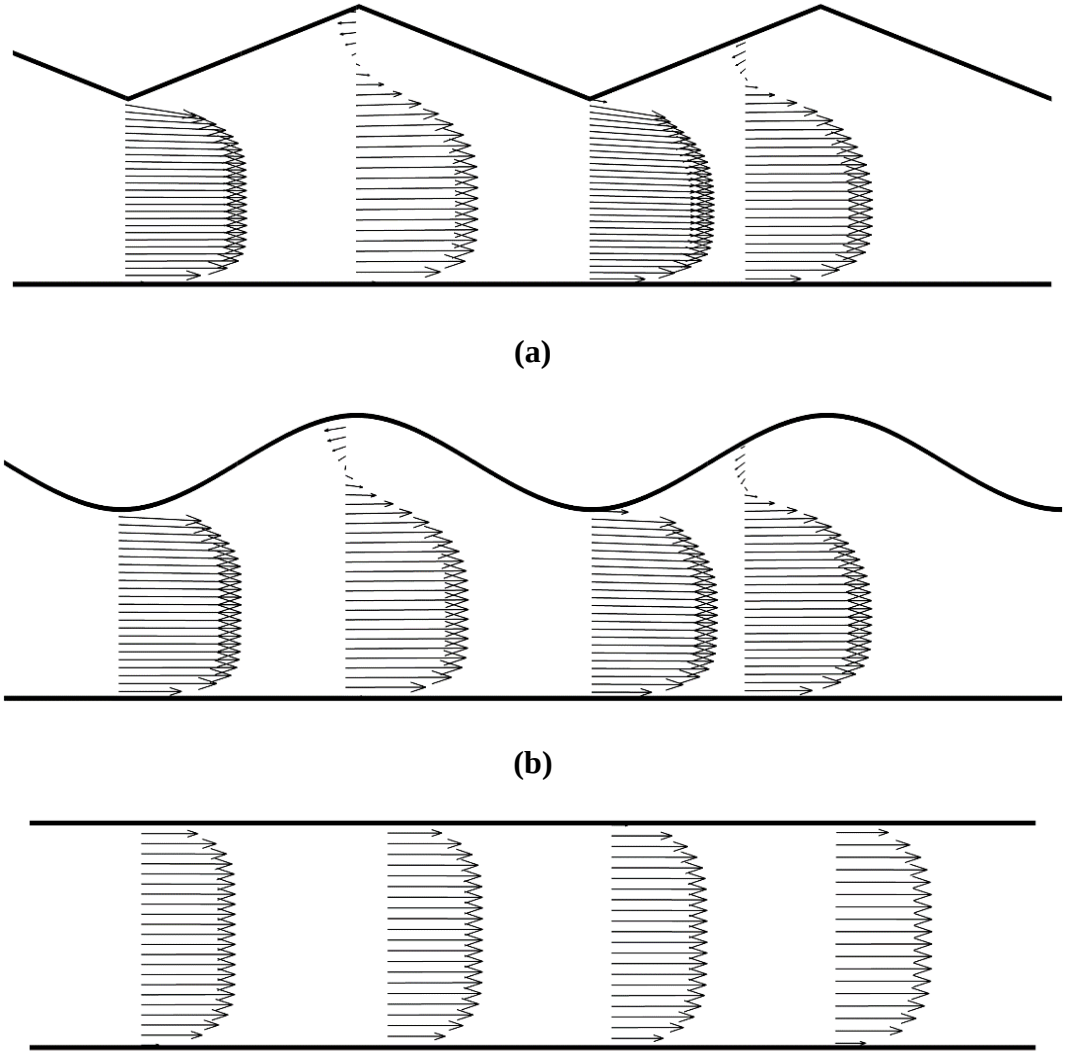

Fig. 6. Average velocity vectors at different sections for (a) triangular channel; (b) sinusoidal channel; (c) straight channel.

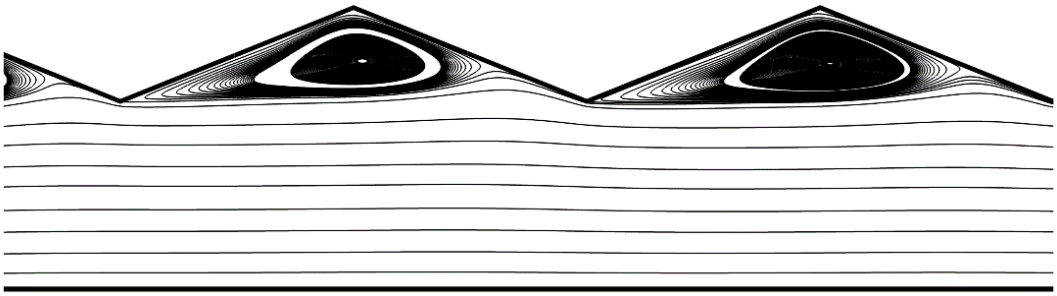

(a)

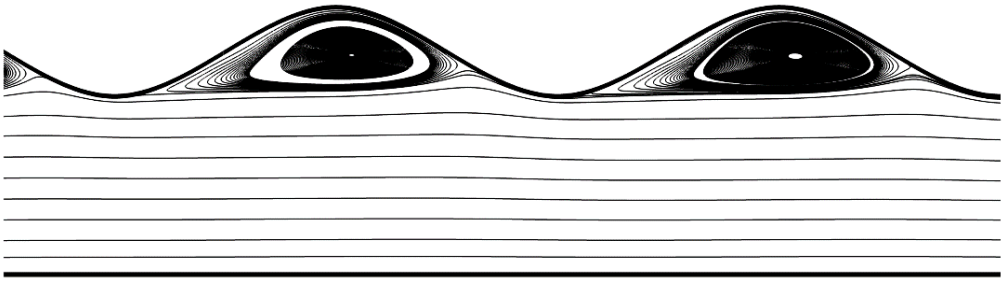

(b)

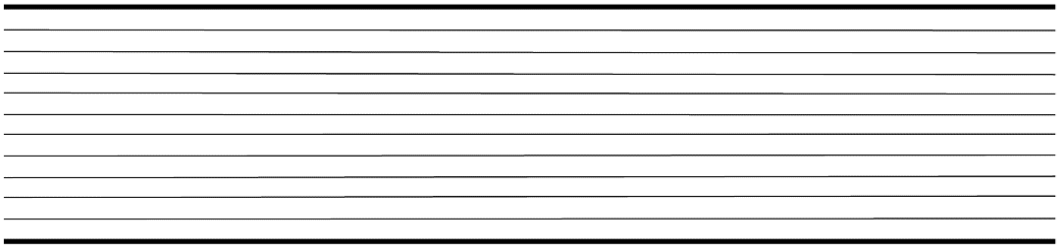

(c)

Fig. 7. Average streamlines for (a) triangular channel; (b) sinusoidal channel; (c) straight channel.

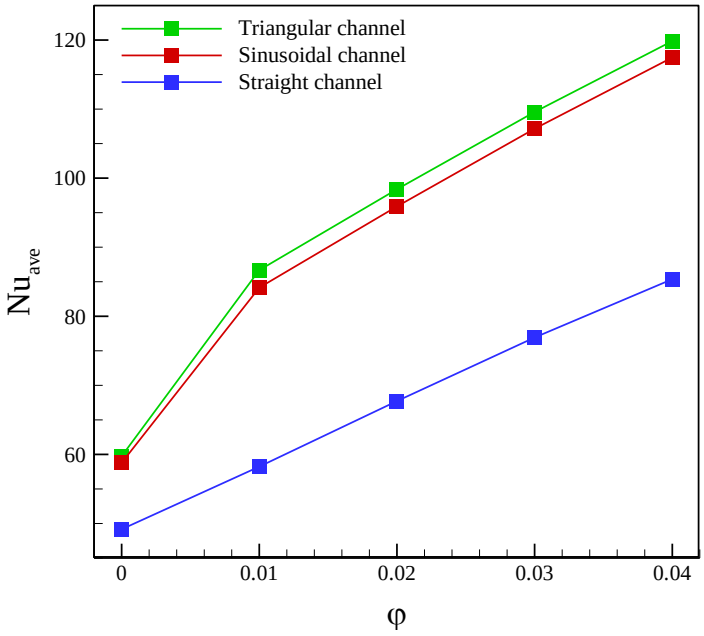

Fig. 8. Variations of the averaged Nusselt number with nanoparticle volume fractions for different channels at Re=5000.

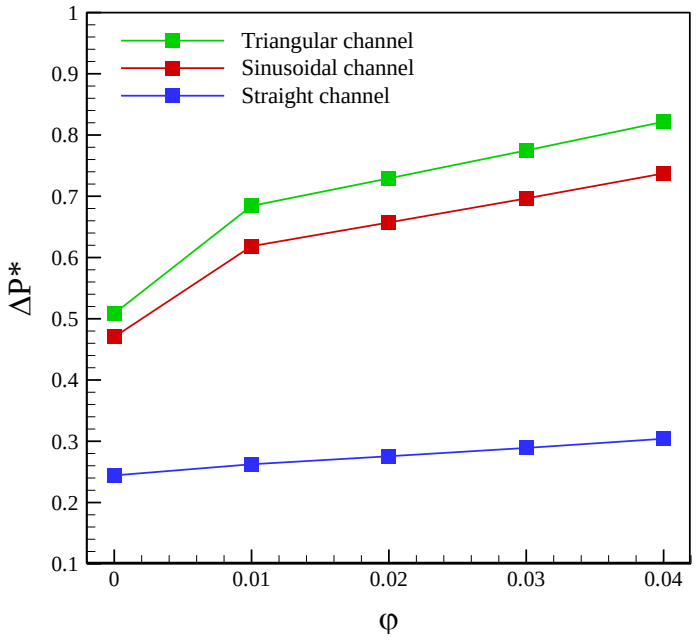

Fig. 9. Variations of non-dimensional pressure drop with nanoparticle volume fractions for different channels at Re=5000.

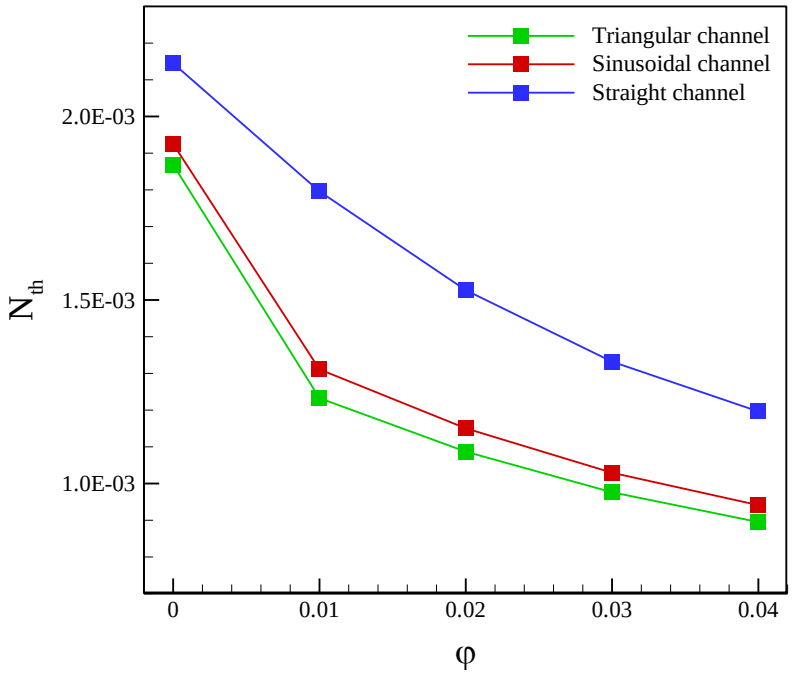

Fig. 10. Variations of non-dimensional thermal entropy generation with nanoparticle volume fractions for different channels at Re=5000.

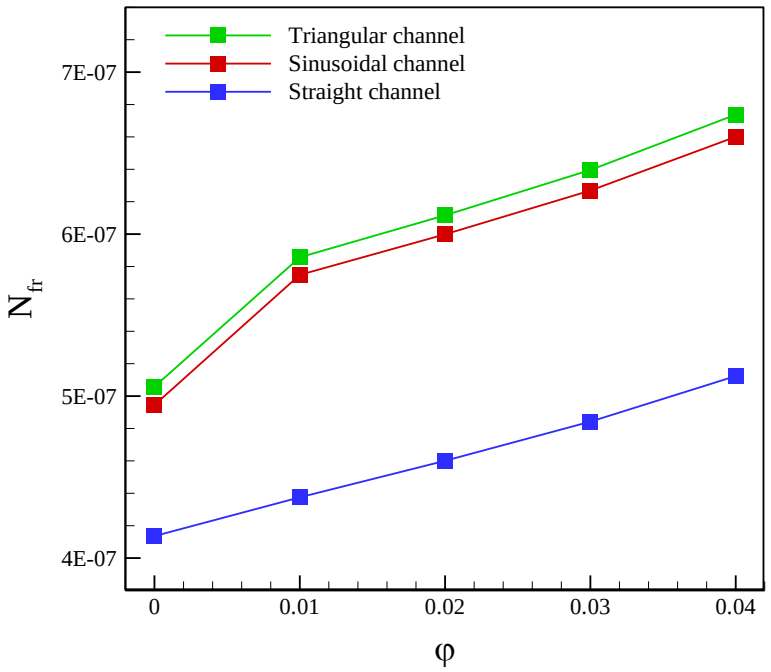

Fig. 11. Variations of non-dimensional frictional entropy generation with nanoparticle volume fractions for different channels at Re=5000.

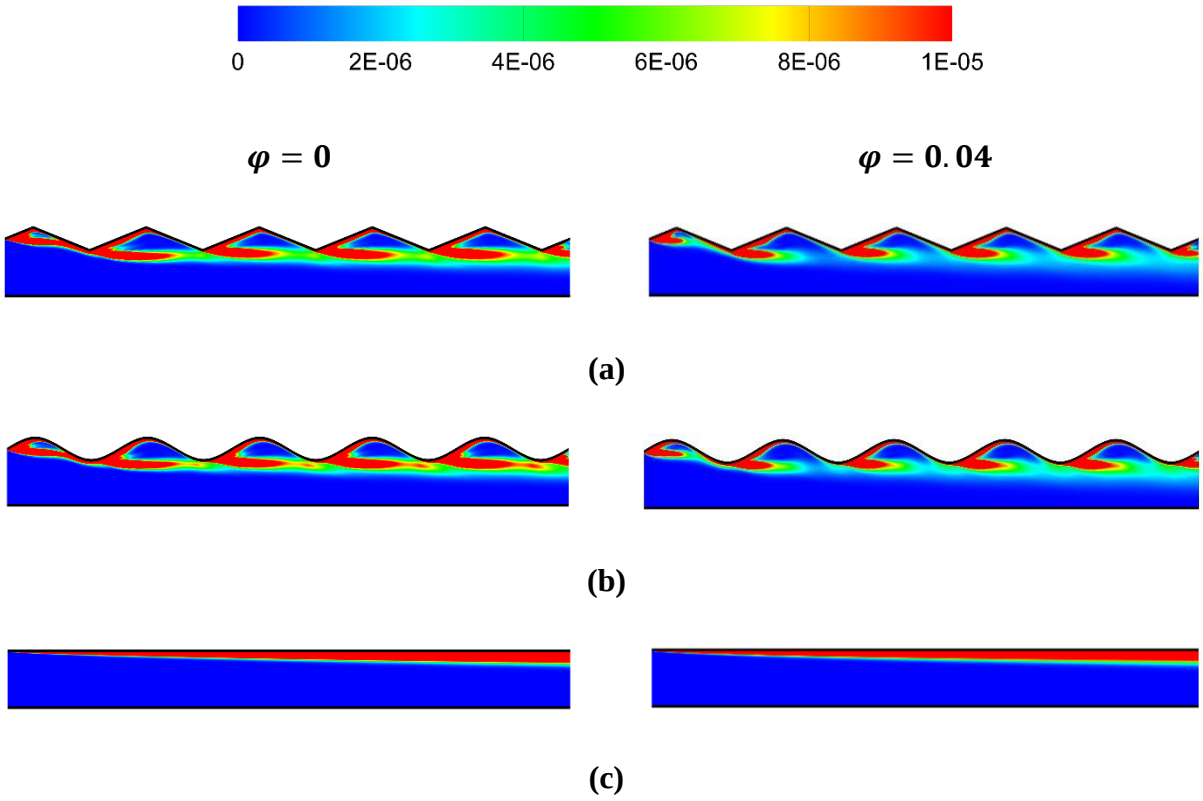

Fig. 12. Non-dimensional thermal entropy generation contours for (a) triangular channel; (b) sinusoidal channel; (c) straight channel at Re=5000.

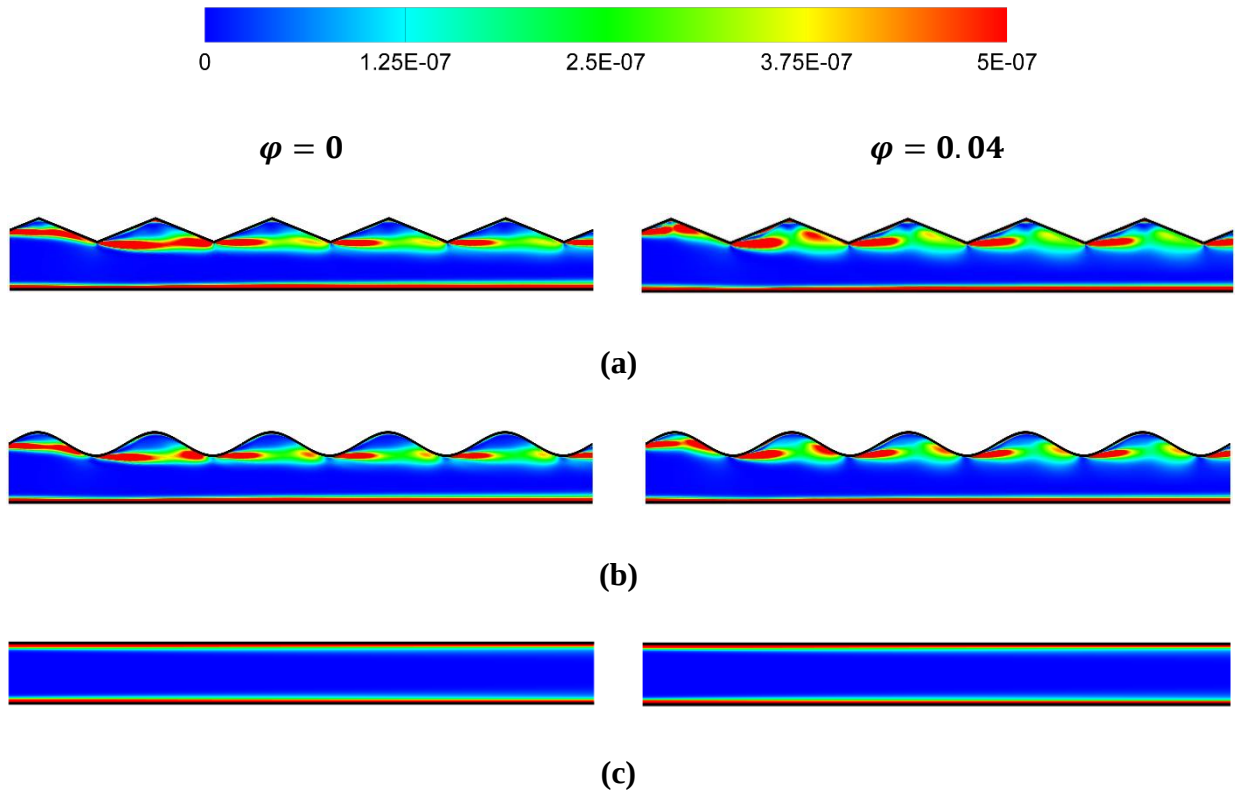

Fig. 13. Non-dimensional frictional entropy generation contours for (a) triangular channel; (b) sinusoidal channel; (c) straight channel at Re=5000.

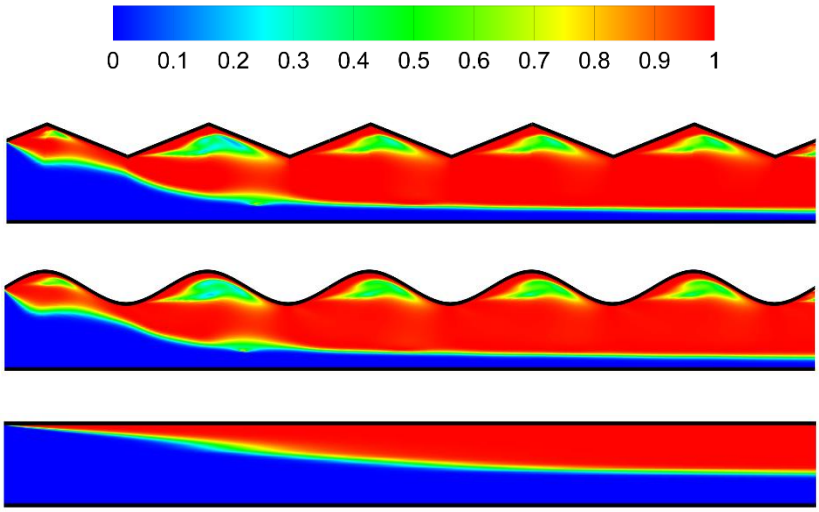

Fig. 14. Bejan number contours at $\varphi = 0.04$ for (a) triangular channel; (b) sinusoidal channel; (c) straight channel

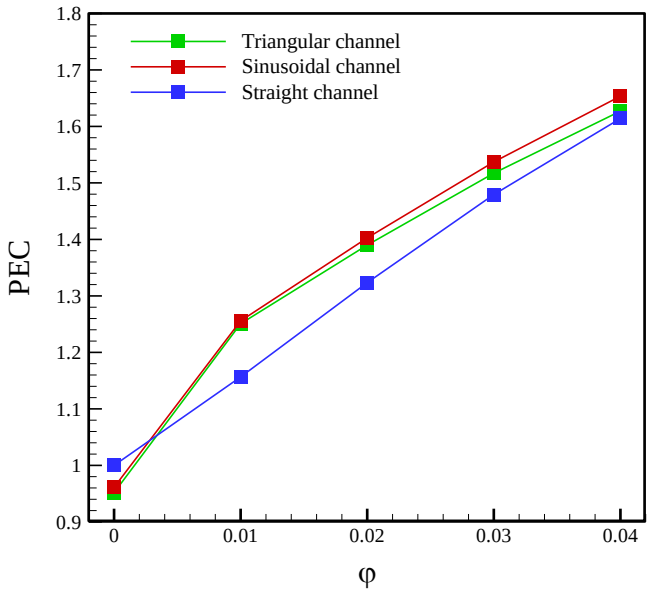

Fig. 15. Variations of PEC with nanoparticle volume fractions for different channels at Re=5000.

Table 1. Physical properties of the base fluid and nanoparticles at 293 K [31]

Material	$\rho\left(\frac{kg}{m^3}\right)$	$\mu\left(\frac{N.m}{s}\right)$	$k\left(\frac{W}{m.K}\right)$	$C_p\left(\frac{J}{kg.K}\right)$
Water	1000	0.001003	0.597	4181.8
Cu	8953	-	386	383.1

Table 2. Comparison between the present numerical results and experimental data of Ahmed et al. [40] for nanofluid flow at $\varphi = 0.01$ in a corrugated channel

	Nu_{ave}		
Re	**Numerical results (present study)**	**Experimental results [28]**	**Percentage difference**
3000	74	65	13.8
4000	102	91	12.1

Table 3. The effects of Reynolds number on heat transfer, pressure drop, PEC, and thermal and frictional irreversibilities for triangular and sinusoidal channels at two values of nanoparticle concentration

Triangular channel						
Re	**4000**		**5000**		**6000**	
$\boldsymbol{\varphi}$	**0.01**	**0.04**	**0.01**	**0.04**	**0.01**	**0.04**
$\boldsymbol{Nu_{ave}}$	74.42	102.3	86.68	119.84	93.37	136.5
$\Delta \boldsymbol{P^*}$	0.7061	0.8453	0.6842	0.8216	0.6687	0.8057
$\boldsymbol{PEC}$	1.312	1.699	1.251	1.627	1.142	1.569
$\boldsymbol{N_{th}}$	0.001450	0.001058	0.001232	0.000895	0.001074	0.000778
$\boldsymbol{N_{fr}}$	3.465e-7	3.999e-7	5.8569e-7	6.7373e-7	8.948e-7	1.023e-6
Sinusoidal channel						
Re	**4000**		**5000**		**6000**	
$\boldsymbol{\varphi}$	**0.01**	**0.04**	**0.01**	**0.04**	**0.01**	**0.04**
$\boldsymbol{Nu_{ave}}$	72.48	100.51	84.14	117.47	91.89	133.63
$\Delta \boldsymbol{P^*}$	0.6456	0.7675	0.6184	0.7373	0.5991	0.7158
$\boldsymbol{PEC}$	1.317	1.724	1.256	1.654	1.166	1.598
$\boldsymbol{N_{th}}$	0.001531	0.001106	0.001311	0.000941	0.001148	0.000821
$\boldsymbol{N_{fr}}$	3.406e-7	3.928e-7	5.7481e-7	6.6003e-7	8.782e-7	9.989e-7